Sharp interface model for solid-state dewetting problems with weakly anisotropic surface energies

Yan Wang,[1] Wei Jiang,[2,*] Weizhu Bao,[1,3] and David J. Srolovitz[4]

[1]*Department of Mathematics, National University of Singapore, Singapore, 119076*

[2]*School of Mathematics and Statistics, Wuhan University, Wuhan 430072, China*

[3]*Center for Computational Science and Engineering, National University of Singapore, Singapore, 119076*

[4]*Departments of Materials Science and Engineering and Mechanical Engineering and Applied Mechanics, University of Pennsylvania, Philadelphia, Pennsylvania 19104, USA*

(Received 28 July 2014; revised manuscript received 13 November 2014; published 12 January 2015)

Based on an energy variational approach, we propose a sharp interface model for simulating solid-state dewetting of thin films with (weakly) anisotropic surface energies. The morphology evolution of thin films is governed by surface diffusion and contact line migration. For the contact line migration, we introduce a relaxation kinetics with a finite contact line mobility by energy gradient flow method. We implement the mathematical model in an explicit finite-difference scheme with cubic spline interpolation for evolving marker points. Following validation of the mathematical and numerical approaches, we simulate the evolution of thin-film islands, semi-infinite films, and films with holes as a function of film dimensions, isotropic Young angle θ_i, anisotropy strength and crystal symmetry, and film crystal orientation relative to the substrate normal. We find that in addition to classical wetting (where holes in a film heal) and dewetting (where holes in a film grow), we observe cases where a hole through the film heals but leaves a finite-size hole/bubble between the continuous film and substrate or where the hole heals leaving a continuous film that is not bonded to the substrate. Surface energy anisotropy (i) increases the instability that leads to island breakup into multiple islands, (ii) enhances hole healing, and (iii) leads to finite island size even under some conditions where the isotropic Young angle θ_i suggests that the film wets the substrate. The numerical results presented in the paper capture many of the complexities associated with solid-state dewetting experiments.

DOI: 10.1103/PhysRevB.91.045303 PACS number(s): 68.35.−p, 68.55.−a, 68.37.−d, 81.16.Rf

I. INTRODUCTION

Solid-state dewetting of thin films on substrates has been observed in a wide range of systems and is of considerable technological interest [1–8]. Unlike dewetting of liquids on substrates, this type of capillarity-driven dewetting occurs primarily through surface diffusion-controlled mass transport at temperatures well below the melting point of the film [1]. In a recent set of experiments, Ye and Thompson [4–7] demonstrated the geometric complexity and importance of crystalline anisotropy in dewetting. These, and related, recent experiments have led to renewed interest in understanding thin-film dewetting and the influence of crystalline anisotropy on dewetting phenomena [9–17].

The morphology evolution of solid-state dewetting can be modeled as a type of surface-tracking problem. In general, the solid-state dewetting process is driven by interfacial energy minimization and occurs through surface diffusion-controlled mass transport process. In addition to being a surface diffusion type of surface-tracking problem, it has the additional feature of a moving contact line. More specifically, the contact line is a triple line (where the film, substrate, and vapor phases meet) that migrates as the surface evolves. Although moving contact line problems have been extensively studied in the fluid mechanics community [18–21], surface diffusion type geometric evolution equations combined with moving contact lines pose a considerable challenge for materials science, applied mathematics, and scientific computing.

Under the assumption that surface energies are isotropic, a mathematical model of solid-state dewetting was first proposed by Srolovitz and Safran [22]. The model can be described in the following Lagrangian representation in two dimensions [22–24]:

$$\frac{\partial \mathbf{X}}{\partial t} = V_n \mathbf{n}, \qquad V_n = B\frac{\partial^2 \mu}{\partial s^2} = B\gamma_{FV}\frac{\partial^2 \kappa}{\partial s^2}, \tag{1}$$

where $\mathbf{X} = (x(s,t), y(s,t))$ represents the moving film front (film/vapor interface) with arc length s and time t, V_n is the moving velocity of the interface in the direction of its outward normal, $\mathbf{n} = (n_1, n_2)$ is the interface outer unit normal direction, the chemical potential $\mu = \gamma_{FV}\kappa$, where γ_{FV} is the surface energy density which is assumed as isotropic (a constant) in the model, and $\kappa = \partial_{ss}x\,\partial_s y - \partial_{ss}y\,\partial_s x$ is the curvature of the interface. The material constant $B = D_s \nu \Omega^2 / k_B T_e$, where D_s is the surface diffusivity, ν is the number of diffusing atoms per unit area, Ω is the atomic volume, $k_B T_e$ is the thermal energy. Because the evolution includes contact point migration, Srolovitz and Safran proposed the following three boundary conditions for moving contact lines [22]:

$$y(x_c, t) = 0, \tag{2a}$$

$$\frac{\partial y/\partial s}{\partial x/\partial s}(x_c, t) = \tan\theta_i, \tag{2b}$$

$$\frac{\partial \mu}{\partial s}(x_c, t) = 0, \tag{2c}$$

where x_c represents the moving contact point where the film, substrate, and vapor meet and θ_i represents the isotropic Young

*Corresponding author: jiangwei1007@whu.edu.cn

angle given by the classical Young equation, i.e., $\cos\theta_i = (\gamma_{VS} - \gamma_{FS})/\gamma_{FV}$, where γ_{FV}, γ_{FS}, and γ_{VS} are, respectively, the surface energy densities of the film/vapor, film/substrate, and vapor/substrate interfaces. Condition (2a) ensures that the contact points always move along the substrate, condition (2b) assumes that the contact angle always keeps fixed as the isotropic Young angle during the evolution, and condition (2c) ensures that the total mass of the thin film is conserved, implying that there is no mass flux at the contact points [23] (please refer to Appendix B for the proof).

Based on the above model, Wong *et al.* [23,25] designed a "marker particle" numerical scheme to study the two-dimensional retraction of a discontinuous film (a film with a step) and the evolution of a perturbed cylindrical wire on a substrate; their numerical experiments indicated that the retracting film edge forms a thickened ridge followed by a valley; with increasing time, the ridge grows in height and the valley sinks, eventually touching the substrate and leading to pinch-off events. Dornel *et al.* [24] developed another numerical scheme to study the two main parameters in this problem: the film aspect ratio and the adhesion energy between the film and substrate, and quantified the retraction rate, breaking time and the number of islands formed. Jiang *et al.* [9] developed a phase field method for simulating solid-state dewetting. The method naturally captures the topological changes that occur during evolution and can be easily extended to three dimensions, avoiding the shortcomings of traditional front-tracking methods.

These earlier studies were based upon the assumption that all interface energies are isotropic. On the other hand, recent experiments have demonstrated that even in the case of cubic metals, crystalline anisotropy can strongly influence dewetting. Therefore, some theoretical models which include the anisotropy are proposed to study the influence of facets on the solid-state dewetting process. For example, Pierre-Louis *et al.* [10–12] applied the kinetic Monte Carlo approach to studying the dewetting of ultrathin solid films. They found a power law of the motion of the dewetting front and the instability is suppressed along faceted orientations. More recently, Zucker *et al.* [13,14] analyzed the important role played by anisotropy during solid-state dewetting based on the crystalline method (Carter *et al.* [26]) applied to a two-dimensional model of edge retraction for highly anisotropic, full-faceted thin films. However, unlike in the isotropic case, valleys do not form ahead of the retracting ridge and hence pinch-off events do not occur in this model. They also did not give an explicit governing equation and boundary conditions for the dewetting. In this paper, we develop a sharp interface model for solid-state dewetting of thin films with weakly anisotropic surface energies.

This paper is organized as follows. First, we present our sharp interface model for simulating solid-state dewetting with anisotropic interface energies including morphology evolution via anisotropic surface diffusion and contact line migration. Then, we perform a series of numerical tests, including numerical stability, contact line mobility, and convergence issues. At last, we apply these results to simulate the morphology evolution of small and large islands on substrates, the retraction and pinch off of semi-infinite films, and the evolution of films with holes with weakly anisotropic surface energies.

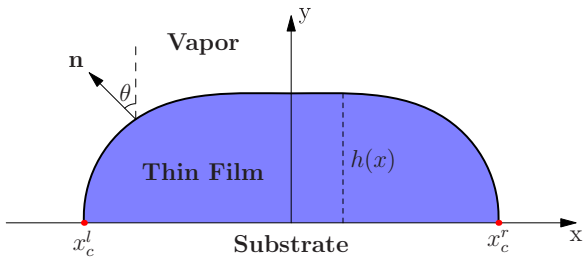

FIG. 1. (Color online) A schematic illustration of a discontinuous solid thin film on a flat, rigid substrate in two dimensions. As the film morphology evolves, the contact points x_c^l and x_c^r move.

II. MODEL FORMULATION

We first present a brief description of the sharp interface model with weakly anisotropic surface energies. Consider the case of a thin solid island on a flat, rigid substrate in two dimensions, as illustrated in Fig. 1. The total free energy of the system can be written as

$$W = \int_{x_c^l}^{x_c^r} \left[\gamma(\theta)\left(1+h_x^2\right)^{1/2} + \gamma_{FS} - \gamma_{VS}\right] dx, \tag{3}$$

where $h = h(x)$ represents the thin-film height [27], x is the horizontal coordinate, $h_x = dh/dx$,θ denotes the interface normal angle related to the film slope by $\cos\theta = 1/(1+h_x^2)^{1/2}$ (see Fig. 1). We assume that the film/vapor interface energy (density) is a function only of the normal angle, i.e., $\gamma_{FV} = \gamma(\theta)$, and x_c^l and x_c^r represent the left- and right-moving contact points, respectively.

We calculate the first variation of the energy functional (3) with respect to the height function $h(x)$ and moving contact points (x_c^l and x_c^r) as (see Appendix A for a more detailed derivation)

$$\frac{\delta W}{\delta h} = (\gamma(\theta) + \gamma''(\theta))\kappa, \quad x \in \left(x_c^l, x_c^r\right), \tag{4}$$

$$\frac{\delta W}{\delta x_c^l} = -[\gamma(\theta)\cos\theta - \gamma'(\theta)\sin\theta + \gamma_{FS} - \gamma_{VS}]_{x=x_c^l}, \tag{5}$$

$$\frac{\delta W}{\delta x_c^r} = [\gamma(\theta)\cos\theta - \gamma'(\theta)\sin\theta + \gamma_{FS} - \gamma_{VS}]_{x=x_c^r}. \tag{6}$$

From Eq. (4), we can define the chemical potential of the system as $\mu = [\gamma(\theta) + \gamma''(\theta)]\kappa$, which is the anisotropic Gibbs-Thomson relation [28]. Note that the term $\widetilde{\gamma}(\theta) = \gamma(\theta) + \gamma''(\theta)$ in μ, called as the surface stiffness, plays an important role in capillarity-driven morphology evolution. As pointed out in Refs. [29,30], spontaneous faceting can occur when $\widetilde{\gamma}(\theta)$ becomes negative for some $-\pi \leqslant \theta \leqslant \pi$. By Fick's laws of diffusion [31], we can define the normal velocity V_n of the moving interface as follows:

$$V_n = B\frac{\partial^2 \mu}{\partial s^2} = B\frac{\partial^2}{\partial s^2}[(\gamma(\theta) + \gamma''(\theta))\kappa]. \tag{7}$$

Analogous to the isotropic case, the above equation can be called as the anisotropic surface diffusion, which governs the motions of "the particles" on the interface away from the contact points.

However, we still need the boundary conditions which govern the movements of the contact points. These can be obtained by calculating the first variation of the total energy functional with respect to the contact points, i.e., Eqs. (5) and (6). We assume that the moving process of the contact points can be taken as the energy gradient flow, which gives the time-dependent Ginzburg-Landau kinetic equations based on a minimization process of the total free energy:

$$\frac{dx_c^l(t)}{dt} = -\eta \frac{\delta W}{\delta x_c^l} \quad \text{at} \quad x = x_c^l, \tag{8}$$

$$\frac{dx_c^r(t)}{dt} = -\eta \frac{\delta W}{\delta x_c^r} \quad \text{at} \quad x = x_c^r, \tag{9}$$

where $\delta W/\delta x_c^l$ and $\delta W/\delta x_c^r$ are given by Eqs. (5) and (6), respectively, and the constant $\eta, 0 < \eta < \infty$ represents contact line mobility, which is a reciprocal of a constant friction coefficient. If $\eta \to \infty$, then $\frac{\delta W}{\delta x_c^l} = -\frac{1}{\eta}\frac{dx_c^l(t)}{dt} \to 0$ and $\frac{\delta W}{\delta x_c^r} = -\frac{1}{\eta}\frac{dx_c^r(t)}{dt} \to 0$ because the moving velocity of contact points must be finite. In this case, Eqs. (8) and (9) collapse to the equation as follows [32]:

$$f(\theta) := \gamma(\theta)\cos\theta - \gamma'(\theta)\sin\theta + \gamma_{FS} - \gamma_{VS} = 0. \tag{10}$$

It can be seen that if the film/vapor interfacial energy is isotropic (i.e., γ is independent of θ), then Eq. (10) reduces to the well-known isotropic Young equation. If the interfacial energy is anisotropic [i.e., $\gamma = \gamma(\theta)$], a bending term $\gamma'(\theta)$ appears which acts perpendicular to the film surface. We refer to Eq. (10) as the anisotropic Young equation. If we adopt Eq. (10) as the boundary conditions, similar to the condition (2b) in the isotropic case, this amounts to assume that the contact angle must keep fixed as a value θ_a which satisfies Eq. (10) during the evolution. However, this approach of fixing the contact angle becomes subtle and unpractical in the anisotropic case because when the surface energy anisotropy increases, Eq. (10) may have multiple solutions. Therefore, we think that it is more reasonable that we adopt Eqs. (8) and (9) as the boundary conditions in the paper.

In addition, the introduction of relaxation kinetics for the contact point position [Eqs. (8) and (9)] has its origin in the complex atomic structure of the contact point, where typically atoms are not all exactly on perfect crystal sites. This variation in the atomic structure in the vicinity of the contact point can be associated with elastic deformation, slipping between film and substrate, dislocations at the film/substrate interface, reconstruction of the interfaces, and other forms of nonelastic deformation. The local distortion of the atomic lattice at the contact point must be propagated along with the moving contact point and because its structure is distinct from that of the remaining film or film/substrate interface it has its own distinct kinetics. Hence, we can think of this contact point as having a unique mobility $M_c = \eta$. A similar concept was introduced to describe the effect of grain boundary triple junctions (where three grain boundaries meet) on the motion of grain boundaries [33,34] and contact lines in liquid film wetting of substrates [18,19,35,36].

Assume that the length and surface energies are scaled by the two constants R_0 and γ_0, respectively. By choosing the time scale to be $R_0^4/(B\gamma_0)$ and the contact line mobility scale to be B/R_0^3, the two-dimensional solid-state dewetting of a thin film on a solid substrate can be described in the following dimensionless form by the sharp interface model:

$$\frac{\partial \mathbf{X}}{\partial t} = V_n \mathbf{n} = \frac{\partial^2 \mu}{\partial s^2}\mathbf{n} = \frac{\partial^2}{\partial s^2}[(\gamma(\theta) + \gamma''(\theta))\kappa]\mathbf{n}. \tag{11}$$

Note that $\mathbf{X}$, t, V_n, s, μ, γ, and η are dimensionless variables, and we still use the same notations for brevity.

The governing equation (11) for the solid-state dewetting problem is subject to the following dimensionless conditions:

(i) Contact point condition (BC1):

$$y(x_c^l, t) = 0, \quad y(x_c^r, t) = 0. \tag{12}$$

(ii) Relaxed (or dissipative) contact angle condition (BC2):

$$\frac{dx_c^l}{dt} = \eta\left[\gamma(\theta_d^l)\cos\theta_d^l - \gamma'(\theta_d^l)\sin\theta_d^l - \cos\theta_i\right], \tag{13}$$

$$\frac{dx_c^r}{dt} = -\eta\left[\gamma(\theta_d^r)\cos\theta_d^r - \gamma'(\theta_d^r)\sin\theta_d^r - \cos\theta_i\right], \tag{14}$$

where θ_i is defined as the isotropic Young contact angle, i.e., $\cos\theta_i = (\gamma_{VS} - \gamma_{FS})/\gamma_0$, θ_d^l and θ_d^r are the (dynamic) contact angle at the left and right contact points, respectively.

(iii) Zero-mass flux condition (BC3):

$$\frac{\partial \mu}{\partial s}(x_c^l, t) = 0, \quad \frac{\partial \mu}{\partial s}(x_c^r, t) = 0, \tag{15}$$

and this condition is necessary for the total mass [denoted as $A(t)$] conservation of the thin film (see more details in Appendix B).

Under the above equations (11)–(15), we can rigorously prove that the total free energy of the system will always decrease during the evolution (please refer to Appendix B). On the other hand, it should be noted that the surface energy anisotropy can be divided into the following two categories according to the value of surface stiffness $\tilde{\gamma}$. One is weak anisotropy when $\tilde{\gamma}(\theta) > 0$ for all surface normal angles θ. In this case, the surface is always smooth during the evolution and the governing equation (11) is mathematically well posed. The other is strong anisotropy when $\tilde{\gamma}(\theta) < 0$ for some ranges of orientation angles θ. In this case, some high-energy surface orientations do not occur, and such surfaces undergo spontaneous faceting, and Eq. (11) becomes an antidiffusion-type equation and so it is ill posed. In this paper, we mainly focus on the weakly anisotropic case. For the strongly anisotropic case, Eq. (11) can be regularized by adding some higher-order terms [37,38], and we will leave it to future studies.

III. NUMERICAL TEST

We solve the governing equations (11)–(15) by an explicit finite-difference method combined with a cubic spline interpolation for evolving marker points (the details are given in Appendix C). Based on the mathematical model and numerical method, we now present the results from several simulations to determine the effect of the contact line mobility η. We then simulate solid-state dewetting in several different thin-film geometries with weakly anisotropic surface energies in two dimensions. For simplicity, we set the initial film thickness

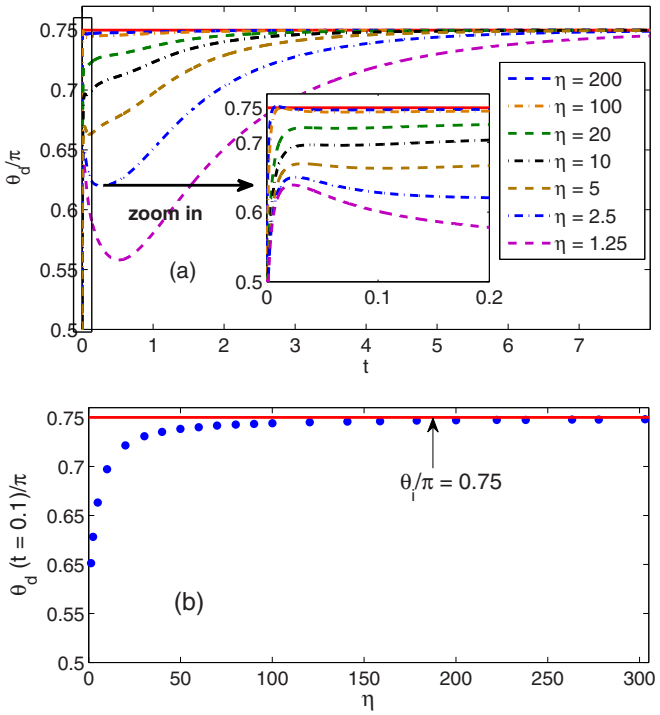

FIG. 2. (Color online) (a) The dynamic contact angle θ_d as a function of time for several different contact line mobilities and simulation parameters $\beta = 0$, $\theta_a = \theta_i = 3\pi/4$ (upper panel). The initial island is rectangular with length $L = 5$, thickness $h = 1$, and $\theta_d(t = 0) = \pi/2$. (b) The dynamic angle θ_d measured at $t = 0.1$ as a function of the contact line mobility η. In the both figures, the red solid lines represent $\theta_a = 3\pi/4$.

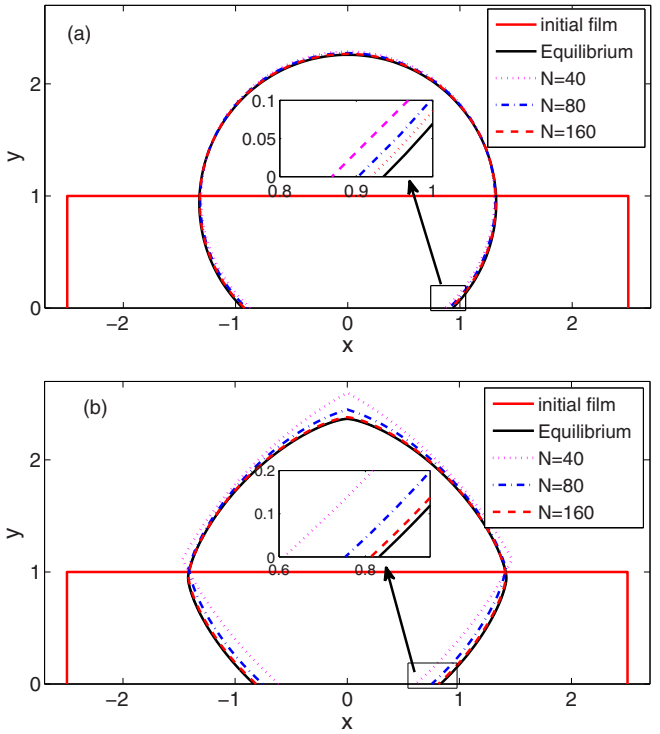

FIG. 3. (Color online) Comparison of the long-time numerical solution of the dynamic island shape with the theoretical equilibrium shape (from the Winterbottom construction, shown in blue) for several values of the number of computational marker points N for (a) the isotropic surface energy case with $\beta = 0$ and $\theta_i = 3\pi/4$ and (b) the weakly surface energy case with $\beta = 0.06$, $\theta_i = 3\pi/4$, and $m = 4$.

to unity, i.e., we choose the length scale R_0 to be the initial film thickness and assume a dimensionless anisotropic surface energy of the form

$$\gamma(\theta) = 1 + \beta\cos[m(\theta + \phi)], \tag{16}$$

where β is the degree of anisotropy, m is the order of the rotational symmetry, and ϕ represents a phase shift angle describing a rotation of the crystallographic axes from a reference orientation (the substrate plane). The surface energy is isotropic for $\beta = 0$ and weakly anisotropic for $0 < \beta < \frac{1}{m^2-1}$. In this paper, ϕ is set to 0, except where noted. In addition, because the numerical scheme presented above is explicit, the time steps in our simulations are always chosen to be of $O[(h^k)^4]$ with h^k the mesh size in the kth time step to ensure numerical stability.

TABLE I. Equilibration times for rectangular islands of thickness $h = 1$ and several initial lengths for different contact line mobilities η (see the text for more details).

η	200	100	20	10
$L = 5$	1.34×10^1	1.35×10^1	1.38×10^1	1.4309×10^1
$L = 100$	1.41×10^3	1.41×10^3	1.41×10^3	1.4094×10^3
Semi-infinite	1.64×10^4	1.64×10^4	1.64×10^4	1.6392×10^4

A. Contact line mobility

The contact line mobility η determines the rate of relaxation of the dynamic contact angle θ_d to the equilibrium contact angle θ_a which satisfies the anisotropic Young equation (10). In general, for small η, the relaxation is very slow and the contact points move very slowly. On the other hand, if η is very large, the relaxation process occurs very quickly such that the dynamic contact angle θ_d quickly converges to θ_a. In this case, the time steps for numerically integrating Eqs. (13) and (14) must be chosen very small in order to maintain numerical stability. From the point of view of numerics, the choice of η must represent a balance between these factors. On the other

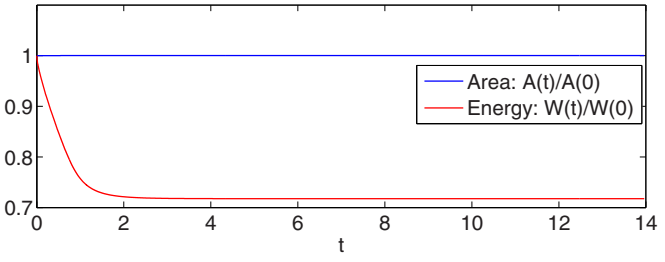

FIG. 4. (Color online) The temporal evolution of the normalized total free energy and the normalized area occupied by the island for the weakly anisotropic case with $N = 80$ and $\beta = 0.06$ presented in Fig. 3(b).

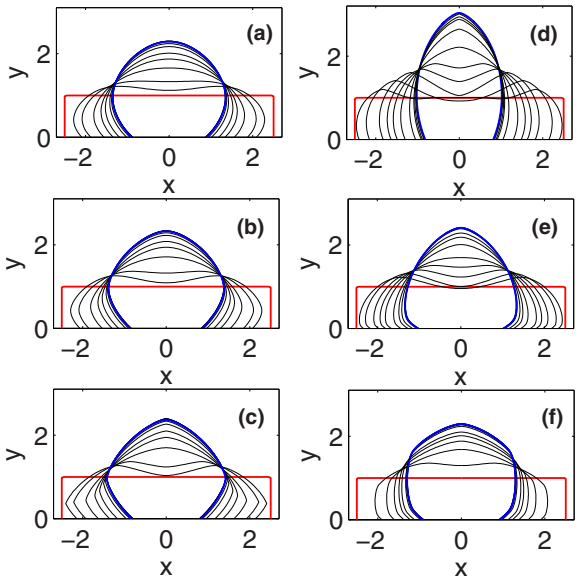

FIG. 5. (Color online) Several steps in the evolution of small, initially rectangular islands (shown in red) toward their equilibrium (Winterbottom) shape (shown in blue) for different anisotropies β and crystalline rotational symmetry orders m ($\theta_i = 3\pi/4$ in all cases). Figures (a)–(c) are results for $\beta = 0.02, 0.04, 0.06$ ($m = 4$ are fixed). Figures (d)– (f) are simulation results for (d) $m = 2$, $\beta = 0.32$, (e) $m = 3$, $\beta = 0.1$, and (f) $m = 6$, $\beta = 0.022$, respectively.

hand, in any physical system, η is a material parameter and must be determined either from experiments or microscopic (e.g., molecular dynamics) simulations.

Figure 2(a) shows the evolution of the dynamic contact angle θ_d as a function of time for seven different mobilities ($\eta = 1.25, 2.5, 5, 10, 20, 100, 200$) for a case of an initially short, thin rectangular island (length $L = 5$, thickness $h = 1$) with $\beta = 0$ and $\theta_i = 3\pi/4$, compared to the anisotropic Young angle $\theta_a = 3\pi/4$ (note that $\theta_a = \theta_i$ in the isotropic case). The contact angle initially grows very quickly from its initial value of $\pi/2$ to a near steady-state dynamical value [see the inset to Fig. 2(a)]. Then, as the island approaches its equilibrium shape, the contact point slows and $\theta_d \to \theta_a$. The near steady-state dynamical angle, seen in the inset for large η, is always smaller than the equilibrium value θ_a and θ_d increases with increasing contact line mobility η [see Fig. 2(b)]. This is consistent with experimental and atomistic simulation observations of the triple junction drag effect on dynamic triple junction angles in grain boundaries [33,34] and in contact lines of fluids on substrates [19,20].

TABLE II. Convergence of the long-time simulation island shape with the theoretical equilibrium shape (Winterbottom construction) as a function of the number of marker points N. The error measures $\alpha_{\rm err}$ and $d_{\rm err}$ are defined in the text.

	Isotropic			Anisotropic		
N	40	80	160	40	80	160
$\alpha_{\rm err}$	0.0721	0.0354	0.0175	0.2644	0.0937	0.0227
$d_{\rm err}$	0.0675	0.0331	0.0163	0.2337	0.0832	0.0189

In order to further clarify the effects of the choice of the mobility η, we performed a series of numerical simulations of the evolution of an initially rectangular, thin-film island ($\beta = 0$, $\theta_i = 3\pi/4$) of three different initial lengths $L = 5$, 100, and semi-infinite, for several values of η and different coefficients. When $L = 5$, the island evolves to an arc of a circle (equilibrium state) and the simulations are terminated when the maximum error in the adjacent time level of marker point separation is smaller than a threshold value. For the $L = 100$ and semi-infinite cases, the simulations are terminated when the first pinch-off event (the film thins to zero thickness creating new contact points) occurs. We compared the results for three different values of $\eta = 10$, 20, 100 and found that η has no discernible effect on the equilibrium island shapes (not shown). η also has very little effect on the simulation termination/island equilibration times (see Table I). For the semi-infinite thin-film case, we numerically computed the contact point position as a function of time and found that it is well described by a power law with the value 0.42, regardless of the contact line mobility η. Unless otherwise noted, the simulations reported below were all performed with $\eta = 100$.

B. Convergence test

We now investigate the convergence of the numerical scheme by performing simulations for a rectangular island of length $L = 5$ and thickness $h = 1$. In this case, the equilibrium island shape can be determined by using the Kaishew approach [39] that is also often referred to as the Winterbottom construction [40] (see Appendix D for more details). We compare the numerical equilibrium island

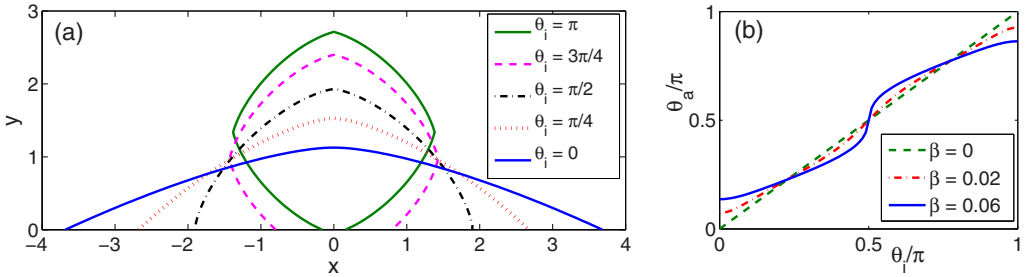

FIG. 6. (Color online) Equilibrium morphologies resulting from the evolution of several small $L = 5$ islands. Figure (a) shows the results for different values of θ_i ($\beta = 0.06, m = 4$). Figure (b) shows the relationship between the anisotropic equilibrium contact angle θ_a and θ_i for different magnitude of anisotropies β.

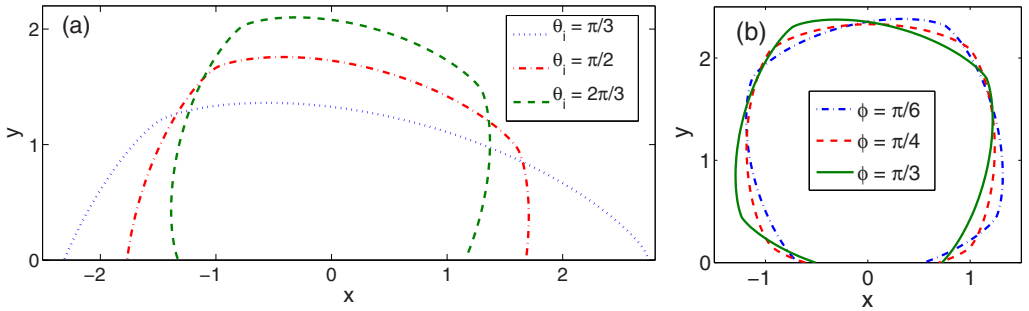

FIG. 7. (Color online) (a) Equilibrium island morphologies for small ($L = 5$) islands with a rotation of the crystal relative to the surface normal of $\phi = \pi/3$ for different values of θ_i. (b) Equilibrium island morphologies for small ($L = 5$) islands with $\theta_i = 5\pi/6$ for several different crystal rotations ϕ (phase shifts). In both figures, $\beta = 0.06$ and $m = 4$.

shape with the theoretical predictions as a function of the number of markers N employed in the description of the island shape. Figure 3 and Table II show the numerical convergence results.

As shown in Fig. 3, the numerical equilibrium states converge to the theoretical equilibrium states (Winterbottom construction, shown by the black curves) with increasing number of marker points from $N = 40$ to 160 in both the isotropic and weakly anisotropic cases; this is a clear demonstration of the convergence of our numerical scheme. We also computed the relative error $\alpha_{\rm err}$ of the right contact point position between the numerical equilibrium state $x^r_{c,n}$ and the theoretical equilibrium state $x^r_{c,e}$, and the maximum distance error $d_{\rm err}$ between the two equilibrium shapes measured by marker points. We define the relative error as $\alpha_{\rm err} = |(x^r_{c,n} - x^r_{c,e})/x^r_{c,e}|$. Table II shows the convergence of the numerical equilibrium shape to the theoretical equilibrium shape. From Table II, we see that the shapes are determined more accurately in the isotropic than in the anisotropic case for the same number of marker points. This can be understood by noting that in the anisotropic surface energy case, more marker points are required to capture the anisotropic morphology than in the smoother isotropic case. In addition, we also computed the temporal evolution of the normalized total free energy $\overline{W}(t)$ and the normalized island size (area) $\overline{A}(t)$ in the weakly anisotropic case shown in Fig. 4 which demonstrates that the area occupied by the island is conserved (mass conservation) during the entire simulation and that the total free energy of the system decays monotonically during the evolution.

IV. ISLAND/FILM EVOLUTION SIMULATION RESULTS

We now examine dewetting in several geometries using the mathematical model described above for weakly anisotropic surface energies. First, we examine the evolution of small islands on a flat substrate with different degrees of anisotropy and m-fold crystal symmetries. Next, we perform numerical simulations for the evolution of large islands and semi-infinite films on a substrate, where pinch off occurs. Then, we examine the relationship among the number of agglomerates resulting from the evolution of islands, the initial island size L, and the isotropic Young angle θ_i. Finally, we examine the evolution of an infinite long thin film containing holes.

A. Small islands

The evolution of small rectangular islands towards their equilibrium shapes is shown in Fig. 5 for several different anisotropy strengths β and m-fold crystalline symmetries for fixed $\theta_i = 3\pi/4$. In all cases, the dynamic contact angle θ_d rapidly converges to the equilibrium contact angle θ_a and then remains fixed throughout the remainder of the island shape evolution. As the anisotropy β increases from 0.02 to 0.06 [Figs. 5(a)–5(c)], the equilibrium island shape changes from smooth and nearly circular to an increasingly anisotropic shape with increasingly sharp corners, as expected based upon the anisotropic surface energy. As the rotational symmetry m [Figs. 5(d)–5(f)] is increased, the number of facets in the equilibrium shape increases.

Figure 6(a) shows the equilibrium shapes of small islands (initially rectangular with $L = 5$, $h = 1$) for different values of the isotropic Young angle $0 \leqslant \theta_i \leqslant \pi$ for $\beta = 0.06$, $m = 4$. Unlike in the isotropic case (even though $\theta_i = 0$ or

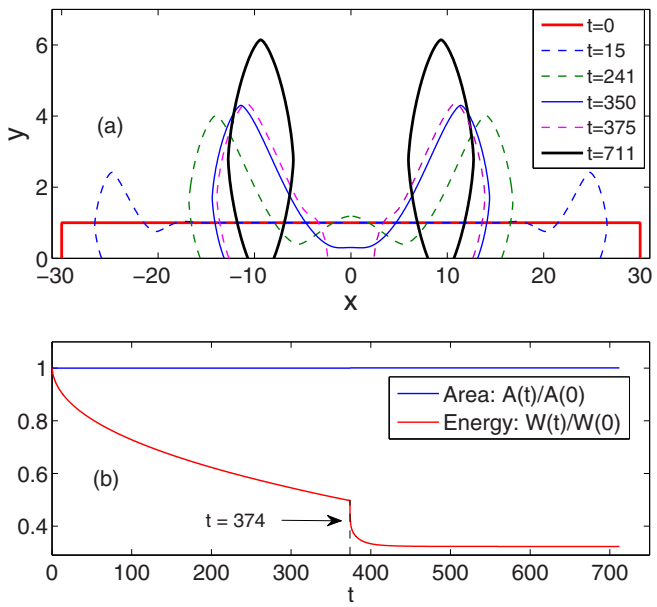

FIG. 8. (Color online) (a) The evolution of a long, thin island (aspect ratio of 60) with weakly anisotropic surface energy ($\beta = 0.06$, $m = 4$, $\theta_i = 5\pi/6$). Note the difference in vertical and horizontal scales. (b) The corresponding temporal evolution of the normalized total free energy and the normalized area (mass).

π), complete wetting (or dewetting) does not occur with anisotropic surface energies. This can be understood by noting that the bending term which appears in the anisotropic Young equation (10) and is absent in its isotropic analog, leading to an equilibrium angle θ_a that differs from θ_i, and is not 0 or π even when $\theta_i = 0$ or π [Fig. 6(b)].

We also performed numerical simulations of the evolution of small islands with finite values of ϕ in Eq. (16) for the weakly anisotropic cases for $\beta = 0.06$, $m = 4$; this corresponds to different rotations of the crystalline axis of the island relative to the substrate normal. The numerical equilibrium shapes for different θ_i and phase shift angles ϕ are shown in Figs. 7(a) and 7(b), respectively. The asymmetry of the equilibrium shapes is clearly seen in the two figures, resulting from breaking the symmetry of the surface energy anisotropy [see Eq. (16)] with respect to the substrate normal. The numerical results confirm that the left and right equilibrium contact angles are two roots of the anisotropic Young equation (10).

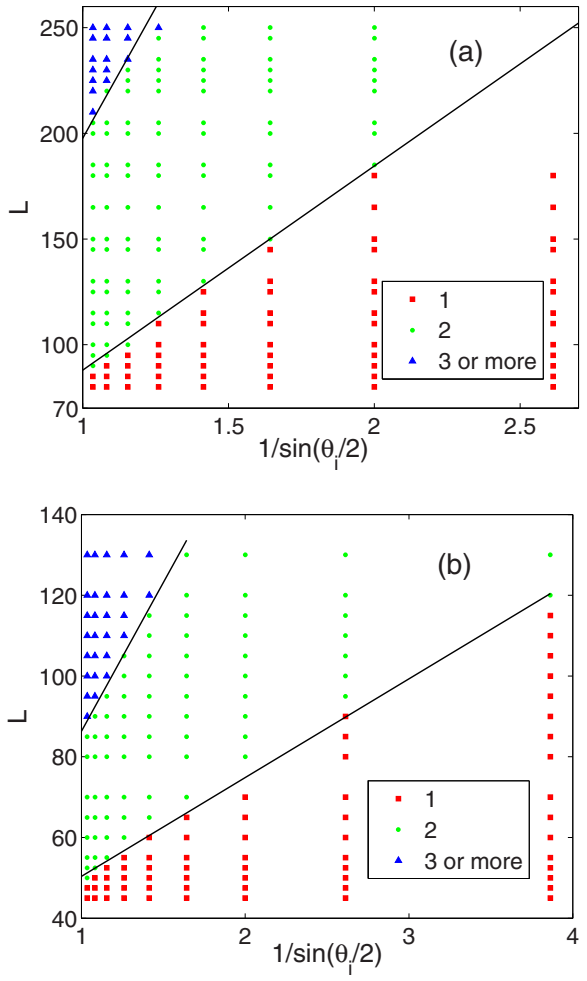

FIG. 9. (Color online) The number of islands formed from the retraction of a high-aspect-ratio island as a function of initial length L and θ_i ($h = 1$) (a) for the isotropic case and (b) anisotropic case with $\beta = 0.06$, $m = 4$. In (a), the solid lines are numerical results of Dornel [24]. In (b), the 1-2 islands and 2-3 islands boundaries (solid lines) are linear curve fittings to our numerical results— $L = 24.46/\sin(\theta_i/2) + 25.91$ and $L = 73.59/\sin(\theta_i/2) + 12.74$, respectively.

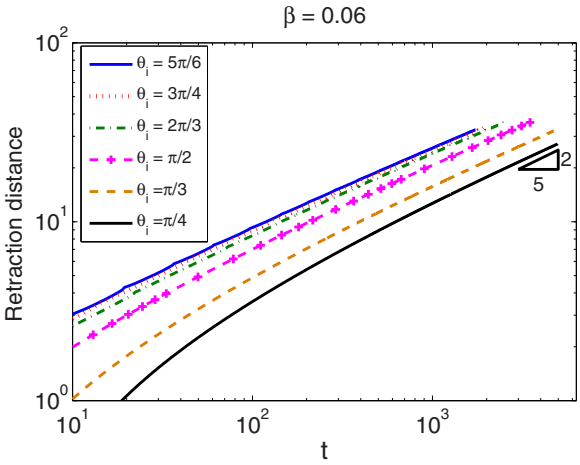

FIG. 10. (Color online) Retraction distance l vs time t for $\beta = 0.06$.

In general, it is possible for a crystal island with an m-fold rotation symmetry to exhibit 0 to $m - 1$ corners upon rotation of the crystal axes with respect to the substrate ϕ and the isotropic Young angle θ_i.

B. Large islands

As noted in the papers [9,24], when the aspect ratios of islands are larger than critical values, the islands pinch off leaving two, three, or more islands. Figure 8(a) shows the temporal evolution of a very large (thin) island (aspect ratio of 60) with weakly anisotropic surface energy. Figure 8(a) shows that surface diffusion kinetics very quickly leads to the formation of ridges at the island edges followed by valleys. As time evolves and the island contact point retracts, these two features become increasing exaggerated, then two valleys merge near the island center. Eventually, the valley at the center of the islands deepens until it touches the substrate, leading to a pinch-off event that separates the initial island into a pair of islands. The corresponding evolution of the normalized total free energy and the normalized enclosed area are shown in

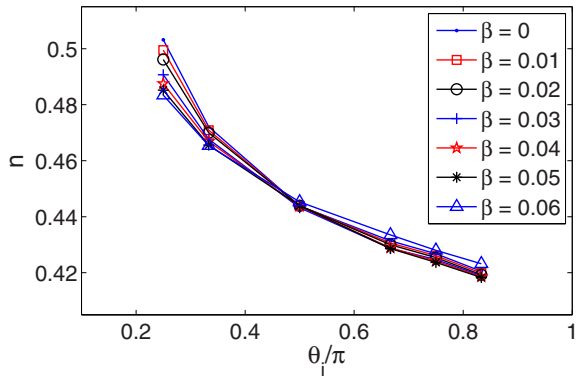

FIG. 11. (Color online) The exponent n obtained by fitting the simulation data for the retraction distance of an initially semi-infinite thin film ($l \sim t^n$) versus the corresponding isotropic Young contact angles θ_i for the case of a weakly anisotropic surface energy with different degrees of anisotropy β.

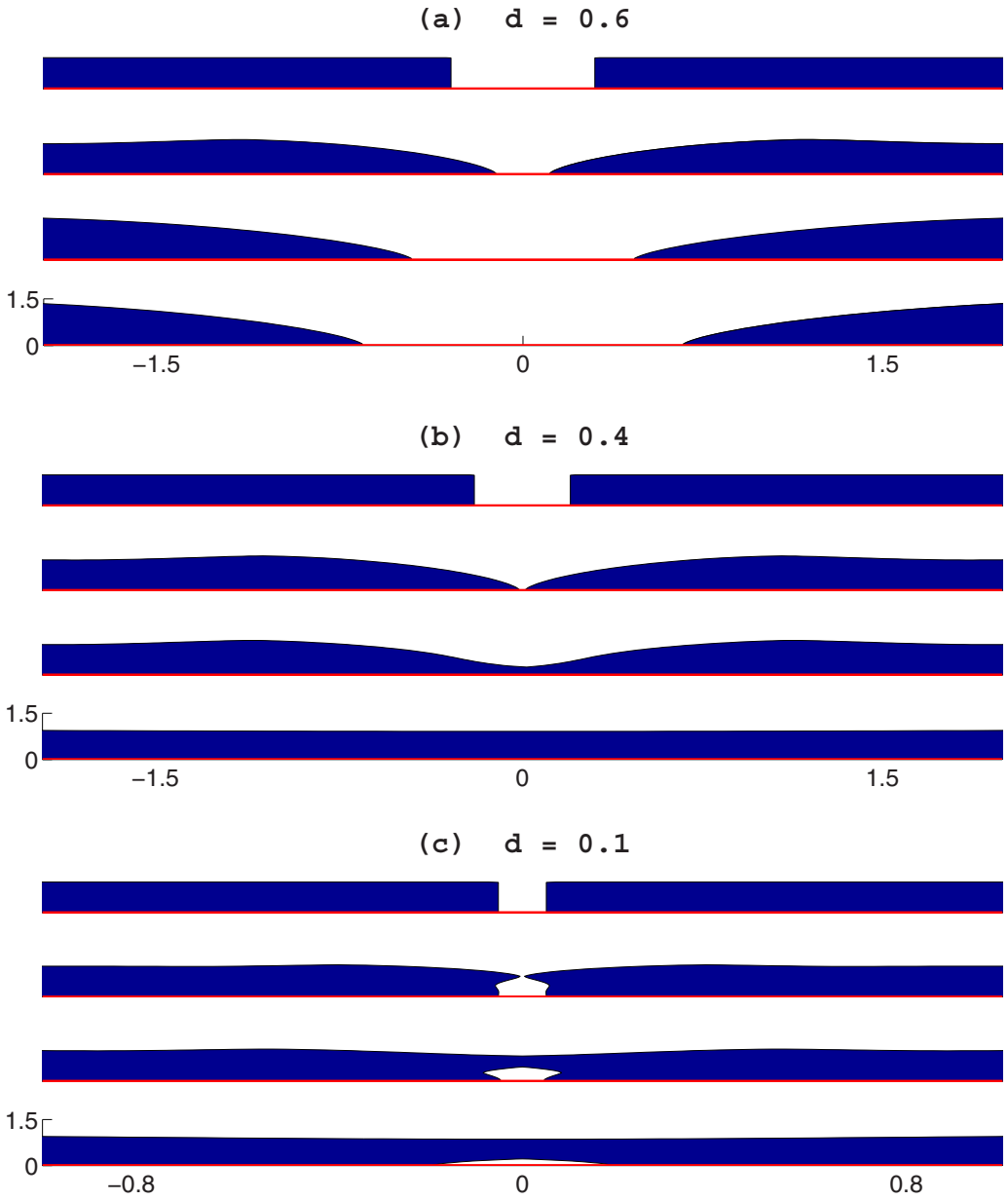

FIG. 12. (Color online) Three different types of morphological evolution of an infinite film with a hole of diameter d under anisotropic surface energy conditions, $\gamma(\theta) = 1 + 0.06\cos(4\theta)$ and $\theta_i = \pi/2$, (a) Case I: dewetting; (b) Case II: wetting; (c) Case III: void. Note that the vertical and horizontal scales are different.

Fig. 8(b). During the dewetting process, the area (mass) is conserved and the energy decays. The energy undergoes a sharp drop at $t = 374$, the moment when the pinch-off event occurs.

In addition to the aspect ratio, the parameter θ_i plays an important role in determining the number of pinch-off events that will occur. We performed a series of numerical simulations for large islands with different aspect ratios and different values of θ_i; the results are shown in Fig. 9 for both the isotropic case and the weakly anisotropic case and we compare these with the results of Dornel [24]. In the numerical results, we observe distinct boundaries between 1, 2, and 3 (or more) islands at late times. For the isotropic case, our numerical results [i.e., the lines that divide between different number of islands, shown in Fig. 9(a)] are consistent with the numerical results of Dornel [24], by observing that in Fig. 9(a) the solid lines represent Dornel's numerical results. For the anisotropic case, our linear curve fittings [shown in Fig. 9(b)] identify that the 1-2 islands and 2-3 islands boundary lines are, respectively, $L = 24.46/\sin(\theta_i/2) + 25.91$ and $L = 73.59/\sin(\theta_i/2) + 12.74$, and these results are different from the numerical results of Dornel. This is because by comparing our numerical results in the isotropic and anisotropic cases [shown in Figs. 9(a) and 9(b)], we can clearly see that for the same value of θ_i an island tends to evolve into a larger number of islands in the anisotropic case than in the isotropic case, but this conclusion is just the opposite to the

observations of numerical results of Dornel (shown in Fig. 9 of Dornel's paper [24]). This difference of numerical results in the anisotropic case can be probably explained as because we used the relaxed contact angle boundary conditions in our model, while they still used the fixed isotropic Young contact angle conditions during the evolution.

C. Semi-infinite films

Several earlier studies have shown that a discontinuous film (i.e., a semi-infinite film) retracts such that the retraction distance scales with time according to a power-law relation $l \sim t^n$ for sufficiently long time. For the isotropic case, analytical predictions in the small film surface slope limit suggest $n = \frac{1}{4}$ with logarithmic corrections by Srolovitz [22] and $n = \frac{2}{5}$ by Wong [23]. On the other hand, numerical simulations using the sharp interface model [23] and phase field model [9] both suggest that $n \approx 0.4$ in the isotropic limit. A study of the anisotropic case also found $n \approx 0.4$ in physical experiments on the dewetting of single-crystal nickel films [13] and silicon-on-insulator films [8].

We simulated the evolution of a discontinuous film (semi-infinite flat film with a step) with the anisotropic surface energy $\gamma(\theta) = 1 + \beta\cos(4\theta)$ and observed a power-law retraction rate. Figure 10 shows a typical log-log plot for computing the exponent n of power law under $\beta = 0.06$ with different isotropic Young angles. Figure 11 shows the exponent n as a function of θ_i for different degrees of anisotropy β. As shown in Fig. 11, the power-law exponent n are all in the 0.4–0.5 range, depending on θ_i but nearly independent of the strength of the anisotropy.

D. Infinite films with a hole

Finally, we performed numerical simulations for the evolution of an initially continuous thin film containing a single hole from the free surface to the substrate. As reported previously [9,22], there exists a critical hole size above which the hole gets larger [i.e., Case I, *dewetting*, shown in Fig. 12(a)] or the hole shrinks and closes [Case II, *wetting*, shown in Fig. 12(b)]. Interestingly, we find a third case where the two sides of the hole touch and merge, leaving a covered hole/void/bubble at the continuous film-substrate interface [Case III, *void*, shown in Fig. 12(c)], which is also recently numerically observed by other methods [41]. In this case, if $\theta_a < \pi$, the void is stable and of finite extent, but if $\theta_a = \pi$, the void will grow leaving a continuous film disconnected from the substrate. We note that the case applies for $f(\theta) > 0$ for all θ [see Eq. (10) for definition of $f(\theta)$]. The occurrence of these three behaviors depends on θ_i (or θ_a) and the initial size of the hole. Figure 13 shows the phase diagram for the relation among the occurrence of the three cases, the parameters θ_i and the initial hole size d for the isotropic and anisotropic surface energy cases. As revealed by the figure, it is easier to form a void at the interface (Case III) for thin films with anisotropic surface energy than when the surface energy is isotropic under the same conditions.

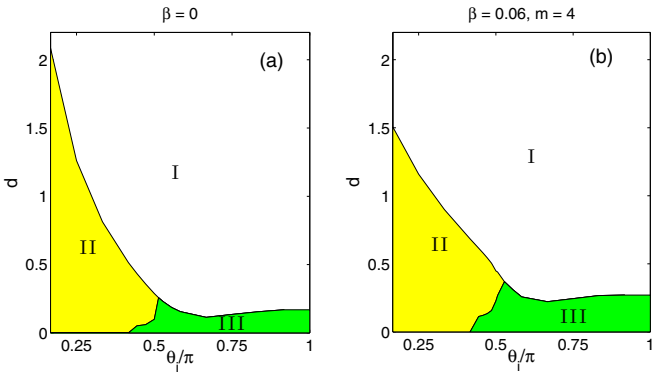

FIG. 13. (Color online) Diagram showing the conditions (d and θ_i) for the occurrence of the three cases: I, *dewetting*; II, *wetting;* and III,*void* for (a) isotropic and (b) anisotropic surface energies (shown by Fig. 12).

V. CONCLUSIONS

In this paper, we described a sharp interface model for simulating solid-state dewetting of thin films with weakly anisotropic surface energy. The evolution of the films is governed by surface diffusion and contact line migration. The derivation of the sharp interface model is based on an energy variational approach. Unlike other sharp interface models, we included a finite contact line mobility during the contact line migration. This gives rise to dynamic contact angles that may be different from the equilibrium contact angles from the Young equation. Many observations have been made of dynamic triple junction angles in grain boundary migration and contact line angles in liquid wetting of substrates that differ markedly from static equilibrium contact angles. We proposed a numerical approach, based upon an explicit finite-difference scheme combined with the cubic spline interpolation for evolving marker points, for solving the sharp interface model. Numerical results for solid-state dewetting in two dimensions demonstrate the excellent performance of the method, including stability, convergence, and numerical efficiency.

With the validated mathematical and numerical approaches, we simulated the evolution of thin-film islands, semi-infinite films, and films with holes as a function of film dimensions, isotropic Young angle θ_i, anisotropy strength and symmetry, and film crystal orientation relative to the substrate normal. Like others, we found that contact point retraction rate can be well described by a power law $l \sim t^n$. Our results demonstrate that the exponent n is sensitive to the isotropic Young angle θ_i (and insensitive to anisotropy). We have also observed that in addition to classical wetting (where holes in a film heal) and dewetting (where holes in a film grow), another possibility is where the holes heal leaving a continuous film but with a void at the film/substrate interface which can be of finite or infinite extent. Surface energy anisotropy was also shown to (i) increase the instability that leads to island breakup into multiple islands, (ii) enhance hole healing, and (iii) lead to finite island size even under some conditions where the isotropic Young angle θ_i suggests that the film wets the substrate. The numerical results presented in the paper capture many of the complexities associated with solid-state dewetting experiments [1,4–7,13].

While, in the present model, we focused on the weakly anisotropic case, the model is readily generalizable to the

strongly anisotropic case. In the strongly anisotropic case, the anisotropic evolution equation (11) becomes ill-posed; this can be simply overcome by adopting a regularization approach [30,37,38] to make it well-posed and/or incorporating a more advanced numerical technique [42–44] that leads to efficient implementations. The contact line mobility approach, developed above, can be applied to the contact line boundary conditions in the strongly anisotropic case.

ACKNOWLEDGMENTS

The authors would like to thank the anonymous referees for helpful comments. This work was supported by the National Natural Science Foundation of China Grant No. 11401446 (W.J.) and the Singapore A*STAR SERC PSF Grant No. 1321202067 (Y.W. and W.B.). Part of the work was done when the authors were visiting Beijing Computational Science Research Center in 2014.

APPENDIX A: DERIVATION OF THE FIRST VARIATION OF THE FREE ENERGY

Denoting δ as the variation of a functional, applying it to variations of the free energy W in Eq. (3), and using the integration by parts, we get

$$\begin{aligned}
\delta W &= \int_{x_c^l}^{x_c^r}\left[\left(1+h_x^2\right)^{1/2}\frac{d\gamma}{dh_x}+\frac{\gamma h_x}{\left(1+h_x^2\right)^{1/2}}\right](\delta h_x)dx+\left[\gamma\left(1+h_x^2\right)^{1/2}+\gamma_{FS}-\gamma_{VS}\right]_{x=x_c^r}\delta x_c^r\\
&\quad-\left[\gamma\left(1+h_x^2\right)^{1/2}+\gamma_{FS}-\gamma_{VS}\right]_{x=x_c^l}\delta x_c^l,\\
&=-\int_{x_c^l}^{x_c^r}\left[\left(1+h_x^2\right)^{1/2}h_{xx}\frac{d^2\gamma}{dh_x^2}+\frac{2h_xh_{xx}}{\left(1+h_x^2\right)^{1/2}}\frac{d\gamma}{dh_x}+\frac{\gamma h_{xx}}{\left(1+h_x^2\right)^{3/2}}\right](\delta h)dx\\
&\quad+\left[\left(1+h_x^2\right)^{1/2}\frac{d\gamma}{dh_x}+\frac{\gamma h_x}{\left(1+h_x^2\right)^{1/2}}\right]_{x=x_c^r}(\delta h)\Big|_{x=x_c^r}-\left[\left(1+h_x^2\right)^{1/2}\frac{d\gamma}{dh_x}+\frac{\gamma h_x}{\left(1+h_x^2\right)^{1/2}}\right]_{x=x_c^l}(\delta h)\Big|_{x=x_c^l}\\
&\quad+\left[\gamma\left(1+h_x^2\right)^{1/2}+\gamma_{FS}-\gamma_{VS}\right]_{x=x_c^r}\delta x_c^r-\left[\gamma\left(1+h_x^2\right)^{1/2}+\gamma_{FS}-\gamma_{VS}\right]_{x=x_c^l}\delta x_c^l\\
&=-\int_{x_c^l}^{x_c^r}\left[\left(1+h_x^2\right)^{1/2}h_{xx}\frac{d^2\gamma}{dh_x^2}+\frac{2h_xh_{xx}}{\left(1+h_x^2\right)^{1/2}}\frac{d\gamma}{dh_x}+\frac{\gamma h_{xx}}{\left(1+h_x^2\right)^{3/2}}\right](\delta h)dx\\
&\quad+\left[\frac{\gamma}{\left(1+h_x^2\right)^{1/2}}-h_x\left(1+h_x^2\right)^{1/2}\frac{d\gamma}{dh_x}+\gamma_{FS}-\gamma_{VS}\right]_{x=x_c^r}\delta x_c^r-\left[\frac{\gamma}{\left(1+h_x^2\right)^{1/2}}-h_x\left(1+h_x^2\right)^{1/2}\frac{d\gamma}{dh_x}+\gamma_{FS}-\gamma_{VS}\right]_{x=x_c^l}\delta x_c^l,
\end{aligned}\tag{A1}$$

where δx_c^r and δx_c^l denote the variations of the free energy with respect to the positions of the right and left contact points and we have used $(\delta h)|_{x=x_c^r}=-h_x|_{x=x_c^r}\delta x_c^r$ and $(\delta h)|_{x=x_c^l}=-h_x|_{x=x_c^l}\delta x_c^l$. Making use of these results, we find the first variation of the total energy functional with respect to $h(x),x_c^r,x_c^l$:

$$\frac{\delta W}{\delta h}=-\left[\left(1+h_x^2\right)^{1/2}h_{xx}\frac{d^2\gamma}{dh_x^2}+\frac{2h_xh_{xx}}{\left(1+h_x^2\right)^{1/2}}\frac{d\gamma}{dh_x}+\frac{\gamma h_{xx}}{\left(1+h_x^2\right)^{3/2}}\right],\quad x\in\left(x_c^l,x_c^r\right)\tag{A2}$$

$$\frac{\delta W}{\delta x_c^r}=\left[\frac{\gamma}{\left(1+h_x^2\right)^{1/2}}-h_x\left(1+h_x^2\right)^{1/2}\frac{d\gamma}{dh_x}+\gamma_{FS}-\gamma_{VS}\right]_{x=x_c^r},\tag{A3}$$

$$\frac{\delta W}{\delta x_c^l}=-\left[\frac{\gamma}{\left(1+h_x^2\right)^{1/2}}-h_x\left(1+h_x^2\right)^{1/2}\frac{d\gamma}{dh_x}+\gamma_{FS}-\gamma_{VS}\right]_{x=x_c^l}.\tag{A4}$$

Introducing the surface normal angle θ, then we immediately have the following relations:

$$\cos\theta=\frac{1}{\left(1+h_x^2\right)^{1/2}},\quad \gamma'(\theta)=\left(1+h_x^2\right)\frac{d\gamma}{dh_x},\tag{A5}$$

$$\gamma''(\theta)=\left(1+h_x^2\right)^2\frac{d^2\gamma}{dh_x^2}+2h_x\left(1+h_x^2\right)\frac{d\gamma}{dh_x},\tag{A6}$$

$$\kappa=-\frac{h_{xx}}{\left(1+h_x^2\right)^{3/2}}.\tag{A7}$$

Inserting Eqs. (A5)–A7 into (A2)–(A4), we obtain the variations used in Eqs. (4)–(6).

APPENDIX B: MASS CONSERVATION AND ENERGY DISSIPATION

Denote $\mathbf{X}(s,t)=(x(s,t),y(s,t))$ as the moving film front with arc length s and time t. As the film evolves, the total length of the interface [denoted as $L(t)$] changes and so the arc length s ($s\in[0,L(t)]$) also changes with time. For simplicity, we introduce a new variable p, which is independent of

time t, to parametrize the moving film/vapor interface, i.e. $s = s(p,t), p \in [0,1]$. Therefore, $p = 0$ and 1 can be used to represent the left and right contact points, respectively. In addition, $\mathbf{n}$ and $\boldsymbol{\tau}$ denote the outer unit normal vector and unit tangent vector, respectively.

Proof of mass conservation. The area(mass) of the thin film is defined as

$$A(t) = \int_0^1 y x_p \, dp.$$

Then, the change rate of the area can be calculated as

$$\begin{aligned}
\frac{dA}{dt} &= \int_0^1 (y_t x_p + y x_{pt}) dp \\
&= \int_0^1 (y_t x_p - y_p x_t) dp + y x_t \Big|_{p=0}^{p=1} \qquad \text{(B1)} \\
&= \int_0^1 (x_t, y_t)(-y_p, x_p) dp \\
&= \int_0^{L(t)} \mathbf{X}_t \cdot \mathbf{n} \, ds \\
&= \int_0^{L(t)} \mu_{ss} ds \\
&= \mu_s(L(t),t) - \mu_s(0,t) = 0. \qquad \text{(B2)}
\end{aligned}$$

Note that in step (B1) we have used integration by parts and the condition that the contact points move along the substrate, i.e., $y(p = 0,t) = y(p = 1,t) = 0$. From the above formulations, we can see that the zero-mass flux conditions (15) or (2c) ensure that the Eq. (B2) is valid.

Hence, the total area (or mass) of the thin film is conserved during the evolution. ■

Proof of energy dissipation. According to Eq. (3), the dimensionless total free energy of the system can be written as follows:

$$W(t) = \int_0^1 \gamma(\theta) s_p \, dp - \left(x_c^r - x_c^l\right) \cos\theta_i,$$

where the variables discussed here are dimensionless and θ_i represents the isotropic Young contact angle

$$\cos\theta_i = \frac{\gamma_{VS} - \gamma_{FS}}{\gamma_0},$$

$$s_p = \frac{\partial s}{\partial p} = \left(x_p^2 + y_p^2\right)^{1/2} = (\mathbf{X}_p \cdot \mathbf{X}_p)^{1/2}.$$

Note that the following equations hold:

$$s_{pt} = \frac{x_p x_{pt} + y_p y_{pt}}{\left(x_p^2 + y_p^2\right)^{1/2}} = \frac{1}{s_p} \mathbf{X}_{pt} \cdot \mathbf{X}_p = \mathbf{X}_{pt} \cdot \boldsymbol{\tau},$$

$$\theta = \arctan \frac{y_p}{x_p}, \quad \theta_p = -\kappa s_p, \quad \theta_t s_p = \mathbf{X}_{pt} \cdot \mathbf{n}.$$

We can calculate the change rate of the total free energy as follows:

$$\begin{aligned}
\frac{dW}{dt} &= \int_0^1 [\gamma'(\theta)\theta_t s_p + \gamma(\theta) s_{pt}] \, dp - \left(\frac{dx_c^r}{dt} - \frac{dx_c^l}{dt}\right) \cos\theta_i \\
&= \int_0^1 \mathbf{X}_{pt} \cdot [\gamma'(\theta)\, \mathbf{n} + \gamma(\theta)\, \boldsymbol{\tau}] \, dp \qquad \text{(B3)} \\
&\quad - \left(\frac{dx_c^r}{dt} - \frac{dx_c^l}{dt}\right) \cos\theta_i \\
&= -\int_0^1 \mathbf{X}_t \cdot [(\gamma''(\theta)\theta_p \mathbf{n} + \gamma'(\theta)\kappa s_p \boldsymbol{\tau}) \\
&\quad + (\gamma'(\theta)\theta_p \boldsymbol{\tau} - \gamma(\theta)\kappa s_p \mathbf{n})] \, dp \qquad \text{(B4)} \\
&\quad + [\mathbf{X}_t \cdot (\gamma'(\theta)\, \mathbf{n} + \gamma(\theta)\, \boldsymbol{\tau})]_{p=0}^{p=1} \\
&\quad - \left(\frac{dx_c^r}{dt} - \frac{dx_c^l}{dt}\right) \cos\theta_i \\
&= \int_0^{L(t)} \kappa(\gamma(\theta) + \gamma''(\theta)) \mathbf{X}_t \cdot \mathbf{n} \, ds \\
&\quad + \frac{dx_c^r}{dt} (\gamma(\theta)\cos\theta - \gamma'(\theta)\sin\theta - \cos\theta_i)_{\theta=\theta_d^r} \\
&\quad - \frac{dx_c^l}{dt} (\gamma(\theta)\cos\theta - \gamma'(\theta)\sin\theta - \cos\theta_i)_{\theta=\theta_d^l} \\
&= \int_0^{L(t)} \mu \mu_{ss} \, ds - C\left[\left(\frac{dx_c^r}{dt}\right)^2 + \left(\frac{dx_c^l}{dt}\right)^2\right] \qquad \text{(B5)} \\
&= \mu \mu_s \Big|_{s=0}^{s=L(t)} - \int_0^{L(t)} \mu_s^2 \, ds - C\left[\left(\frac{dx_c^r}{dt}\right)^2 + \left(\frac{dx_c^l}{dt}\right)^2\right] \\
&= -\int_0^{L(t)} \mu_s^2 \, ds - C\left[\left(\frac{dx_c^r}{dt}\right)^2 + \left(\frac{dx_c^l}{dt}\right)^2\right] \leqslant 0, \qquad \text{(B6)}
\end{aligned}$$

where the constant $C = 1/\eta > 0$ for $0 < \eta < \infty$. In the above calculations, we have used integration by parts from step (B3) to step (B4); step (B5) is obtained by making use of the relaxed contact angle boundary conditions (13) and (14); step (B6) is obtained by integration by parts and the zero-mass flux condition (15).

Hence, we have proved that the total free energy of the system is dissipative during the evolution. ■

APPENDIX C: NUMERICAL METHOD

The detailed algorithm at the kth time step is as follows.

First, suppose that there are $N + 1$ marker points uniformly distributed on the film/vapor interface (curve) with respect to the arc length at the time step k. We denote the total arc length of the curve as L^k, the mesh size as $h^k := L^k/N$, the time step as $\mathcal{T}^k$, and the uniformly distributed marker points as (x_j^k, y_j^k), $j = 0,1,\ldots,N$. Evolving the $N + 1$ marker points according to Eqs. (11)–(15) based on the following explicit finite-difference method, we obtain the positions of the $N + 1$ marker points at the time step $k + 1$, denoted as $(\tilde{x}_j^{k+1}, \tilde{y}_j^{k+1}), j = 0,1,\ldots,N$. In addition, we denote $\kappa_j^k, \theta_j^k, \gamma_j^k = \gamma(\theta_j^k)$ and μ_j^k to be approximations to the curvature, the interfacial normal angle, the dimensionless

film/vapor surface energy density, and the chemical potential on the jth marker point at the kth time step. Next, we introduce the following finite-difference discretization operators:

$$\delta_t^+ x_j^k = \frac{\tilde{x}_j^{k+1} - x_j^k}{\mathcal{T}^k},$$
$$\delta_s x_j^k = \frac{x_{j+1}^k - x_{j-1}^k}{2h^k},$$
$$\delta_s^2 x_j^k = \frac{x_{j+1}^k - 2x_j^k + x_{j-1}^k}{(h^k)^2}.$$

Using a central finite-difference scheme for discretizing the spatial derivatives and a forward Euler scheme for discretizing the temporal derivatives, the governing equations (11) become

$$\begin{aligned} \delta_t^+ x_j^k &= -\delta_s^2 \mu_j^k \delta_s y_j^k, \\ \delta_t^+ y_j^k &= \delta_s^2 \mu_j^k \delta_s x_j^k, \qquad j = 1, \ldots, N-1 \\ \mu_j^k &= \left[\gamma_j^k + \gamma''\left(\theta_j^k\right)\right]\kappa_j^k, \\ \kappa_j^k &= \delta_s y_j^k \delta_s^2 x_j^k - \delta_s x_j^k \delta_s^2 y_j^k, \end{aligned} \tag{C1}$$

and the boundary conditions (12)–(15) become

$$\tilde{y}_0^{k+1} = \tilde{y}_N^{k+1} = 0, \tag{C2}$$

$$\delta_t^+ x_0^k = \eta\left[\gamma_0^k \cos\left(\theta_0^k\right) - \gamma'\left(\theta_0^k\right)\sin\left(\theta_0^k\right) - \cos\theta_i\right], \tag{C3}$$

$$\delta_t^+ x_N^k = -\eta\left[\gamma_N^k \cos\left(\theta_N^k\right) - \gamma'\left(\theta_N^k\right)\sin\left(\theta_N^k\right) - \cos\theta_i\right], \tag{C4}$$

$$\mu_0^k = \tfrac{4}{3}\mu_1^k - \tfrac{1}{3}\mu_2^k, \quad \mu_N^k = \tfrac{4}{3}\mu_{N-1}^k - \tfrac{1}{3}\mu_{N-2}^k. \tag{C5}$$

Based on this numerical scheme, we immediately obtain the positions of the marker points $(\tilde{x}_j^{k+1}, \tilde{y}_j^{k+1})$, $j = 0,1,\ldots,N$. Note that these marker points may not be uniformly distributed along the curve with respect to the arc length. Thus, we redistribute these marker points via a cubic spine interpolation such that they are uniformly distributed as follows. First, making use of these new marker points $(\tilde{x}_j^{k+1}, \tilde{y}_j^{k+1})$, $j = 0,1,\ldots,N$, we construct a piecewise curve $\{[X_j^{k+1}(p), Y_j^{k+1}(p)],\ p \in [(j-1)h^k, jh^k]\}_{j=1,2,\ldots,N}$ by using a cubic spline interpolation. Here, $X_j^{k+1}(p)$ and $Y_j^{k+1}(p)$ are cubic polynomials obtained from a cubic spline interpolation for the points $\{(jh^k, \tilde{x}_j^{k+1}),\ j = 0,1,\ldots,N\}$ and $\{(jh^k, \tilde{y}_j^{k+1}),\ j = 0,1,\ldots,N\}$, respectively. By using these cubic polynomials, we directly compute the arc length of each piecewise cubic polynomial curve, denoted as L_j^{k+1}, $j = 1,2,\ldots,N$. Then, we obtain the total arc length $L^{k+1} = \sum_{j=1}^N L_j^{k+1}$ and determine the uniform mesh size at the $(k+1)$th time step as $h^{k+1} = L^{k+1}/N$. In order to redistribute the $N+1$ points uniformly according to the arc length for the $(k+1)$th time step computation, we set $x_0^{k+1} = \tilde{x}_0^{k+1}$, $y_0^{k+1} = \tilde{y}_0^{k+1} = 0$, $x_N^{k+1} = \tilde{x}_N^{k+1}$, $y_N^{k+1} = \tilde{y}_N^{k+1} = 0$. For each fixed $j = 1,2,\ldots,N-1$, we first locate to which unique piecewise cubic polynomial curve the new jth point (x_j^{k+1}, y_j^{k+1}) belongs, i.e., finding a unique $1 \leqslant i \leqslant N$ such that $\sum_{l=1}^{i-1} L_l^{k+1} \leqslant jh^{k+1} < \sum_{l=1}^{i} L_l^{k+1}$, then numerically solve the following equation:

$$\begin{aligned} g(q) &= \int_{(i-1)h^k}^{(i-1)h^k+q} \sqrt{\left(\frac{dX_i^{k+1}(p)}{dp}\right)^2 + \left(\frac{dY_i^{k+1}(p)}{dp}\right)^2}\, dp \\ &= jh^{k+1} - \sum_{l=1}^{i-1} L_l^{k+1}, \quad 0 \leqslant q < h^k \end{aligned}$$

to obtain its unique root $q = q^*$, and finally the position of the jth uniformly distributed marker point at the $(k+1)$th time step is obtained as $x_j^{k+1} = X_i^{k+1}[(i-1)h^k + q^*]$ and $y_j^{k+1} = Y_i^{k+1}[(i-1)h^k + q^*]$.

APPENDIX D: WINTERBOTTOM CONSTRUCTION

In this paper, we use the following form of the chemical potential for the weakly anisotropic surface energy:

$$\mu = [\gamma(\theta) + \gamma''(\theta)]\kappa, \quad \gamma(\theta) = 1 + \beta\cos[m(\theta + \phi)].$$

For simplicity, we assume here that $\phi = 0$. The corresponding Wulff shape (the equilibrium crystal shape without a substrate) for this surface energy can be explicitly written as [30]

$$\begin{aligned} x(\theta) &= -\gamma(\theta)\sin\theta - \gamma'(\theta)\cos\theta, \\ y(\theta) &= \gamma(\theta)\cos\theta - \gamma'(\theta)\sin\theta, \end{aligned} \qquad \theta \in [-\pi, \pi].$$

We note a slight difference in notation as compared to that in Ref. [30]; in Ref. [30], θ is the angle between the surface outer normal and the x axis while here θ is the angle between the surface outer normal and the y axis.

The equilibrium shape for an island on a flat, rigid substrate can be constructed, using the Winterbottom approach [40], by adding a substrate parallel to the x axis to the Wulff shape (above). The distance from the substrate to the Wulff point (center of the Wulff shape) is $|\cos\theta_i|$, i.e., $\cos\theta_i = (\gamma_{VS} - \gamma_{FS})/\gamma_0 \in [-1,1]$. More precisely, if $\theta_i \in (\pi/2, \pi]$, the Wulff point lies within the Wulff shape and the substrate is at $y = \cos\theta_i$ and parallel to the x axis; if $\theta_i \in [0, \pi/2)$, the Wulff point lies outside of the equilibrium shape and the substrate is at $y = \cos\theta_i$ and parallel to the x axis. Therefore, the equilibrium shape of a crystal on a flat substrate which is coincident with the x axis (i.e., at $y = 0$) can be rewritten as

$$\begin{aligned} x(\theta) &= -\gamma(\theta)\sin\theta - \gamma'(\theta)\cos\theta, \\ y(\theta) &= \gamma(\theta)\cos\theta - \gamma'(\theta)\sin\theta - \cos\theta_i, \end{aligned} \qquad \theta \in [-\theta_a, \theta_a]$$

where the equilibrium contact angle $\theta_a \in [0, \pi]$ is determined from

$$\cos(\theta_a) = \left.\frac{(y'(\theta), -x'(\theta)) \cdot (0,1)}{\sqrt{(x'(\theta))^2 + (y'(\theta))^2}}\right|_{y=0} = \left.\cos(\theta)\right|_{y=0}.$$

From this expression, we see that the equilibrium contact angle θ_a can be any root of the equation

$$\gamma(\theta)\cos\theta - \gamma'(\theta)\sin\theta - \cos\theta_i = 0,$$

which satisfies the contact angle equation (10).

Finally, we ensure the conservation of area (or mass) of the crystal by a normalization procedure. Assume that the enclosed area of the equilibrium shape given by the Winterbottom construction above is A_w, i.e., $A_w = -\int_{-\theta_a}^{\theta_a} y(\theta)\, x'(\theta)\, d\theta$, then

the normalized equilibrium shape is explicitly given by

$$x_e(\theta) = -\sqrt{\frac{A_0}{A_w}}[\gamma(\theta)\sin\theta + \gamma'(\theta)\cos\theta], \quad y_e(\theta) = \sqrt{\frac{A_0}{A_w}}[\gamma(\theta)\cos\theta - \gamma'(\theta)\sin\theta - \cos\theta_i],$$

where $\theta \in [-\theta_a,\theta_a]$ and A_0 is the area (or mass) enclosed by the film and substrate.

[1] C. V. Thompson, Annu. Rev. Mater. Res. **42**, 399 (2012).
[2] E. Jiran and C. V. Thompson, J. Electron Mater. **19**, 1153 (1990).
[3] E. Jiran and C. V. Thompson, Thin Solid Films **208**, 23 (1992).
[4] J. Ye and C. V. Thompson, Appl. Phys. Lett. **97**, 071904 (2010).
[5] J. Ye and C. V. Thompson, Phys. Rev. B **82**, 193408 (2010).
[6] J. Ye and C. V. Thompson, Acta Mater. **59**, 582 (2011).
[7] J. Ye and C. V. Thompson, Adv. Mater. **23**, 1567 (2011).
[8] F. Leroy, F. Cheynis, T. Passanante, and P. Muller, Phys. Rev. B **85**, 195414 (2012).
[9] W. Jiang, W. Bao, C. V. Thompson, and D. J. Srolovitz, Acta Mater. **60**, 5578 (2012).
[10] O. Pierre-Louis and Y. Saito, Europhys. Lett. **86**, 46004 (2009).
[11] O. Pierre-Louis, A. Chame, and Y. Saito, Phys. Rev. Lett. **103**, 195501 (2009).
[12] M. Dufay and O. Pierre-Louis, Phys. Rev. Lett. **106**, 105506 (2011).
[13] G. H. Kim, R. V. Zucker, W. C. Carter, and C. V. Thompson, J. Appl. Phys. **113**, 043512 (2013).
[14] R. V. Zucker, J. H. Kim, W. C. Carter, and C. V. Thompson, C. R. Phys. **14**, 564 (2013).
[15] L. Klinger, D. Amram, and E. Rabkin, Scr. Mater. **64**, 962 (2011).
[16] A. Kosinova, L. Klinger, O. Kovalenko, and E. Rabkin, Scr. Mater. **82**, 33 (2014).
[17] E. Rabkin, D. Amram, and E. Alster, Acta Mater. **74**, 30 (2014).
[18] T. Z. Qian, X. P. Wang, and P. Sheng, J. Fluid Mech. **564**, 333 (2006).
[19] W. Ren and W. E, Phys. Fluids **19**, 022101 (2007).
[20] W. Ren, D. Hu, and W. E, Phys. Fluids **22**, 102103 (2010).
[21] W. Ren and W. E, Phys. Fluids **23**, 072103 (2011).
[22] D. J. Srolovitz and S. A. Safran, J. Appl. Phys. **60**, 255 (1986).
[23] H. Wong, P. W. Voorhees, M. J. Miksis, and S. H. Davis, Acta Mater. **48**, 1719 (2000).
[24] E. Dornel, J. C. Barbe, F. deCrecy, G. Lacolle, and J. Eymery, Phys. Rev. B **73**, 115427 (2006).
[25] P. Du, M. Khenner, and H. Wong, J. Comput. Phys. **229**, 813 (2010).
[26] W. C. Carter, A. R. Roosen, J. W. Cahn, and J. E. Taylor, Acta Metall. Mater. **43**, 4309 (1995).
[27] For simplicity of presentation, we assume $h(x)$ is a single-valued function of x. When $h(x)$ is a multivalued function, this procedure is applied using an arc length parametrization.
[28] A. P. Sutton and R. W. Balluffi, *Interfaces in Crystalline Materials* (Clarendon, Oxford, 1996).
[29] W. W. Mullins, J. Math. Phys. **3**, 754 (1962).
[30] J. J. Eggleston, G. B. McFadden, and P. W. Voorhees, Phys. D (Amsterdam) **150**, 91 (2001).
[31] R. W. Balluffi, S. M. Allen, and W. C. Careter, *Kinetics of Materials* (Wiley, London, 2005).
[32] D. H. Min and H. Wong, J. Appl. Phys. **100**, 053523 (2006).
[33] U. Czubayko, V. G. Sursaeva, G. Gottstein, and L. S. Shvindlerman, Acta Mater. **46**, 5863 (1998).
[34] M. Upmanyu, D. J. Srolovitz, L. S. Shvindlerman, and G. Gottstein, Acta Mater. **50**, 1405 (2002).
[35] P. de Gennes, Rev. Mod. Phys. **57**, 827 (1985).
[36] J. Ralston, M. Popescu, and R. Seder, Annu. Rev. Mater. Res. **38**, 23 (2008).
[37] A. Carlo, M. Gurtin, and P. Podio-Guidugli, SIAM J. Appl. Math. **52**, 1111 (1992).
[38] S. Torabi, J. S. Lowengrub, A. Voigt, and S. Wise, Proc. R. Soc. London, Ser. A **465**, 1337 (2010).
[39] R. Kaishew, Commun. Bulg. Acad. Sci. **1**, 100 (1950).
[40] W. L. Winterbottom, Acta Metall. **15**, 303 (1967).
[41] V. Derkach, A. Novick-Cohen, and E. Rabkin (private communication).
[42] T. Y. Hou, J. S. Lowengrub, and M. J. Shelley, J. Comput. Phys. **114**, 312 (1994).
[43] J. W. Barrett, H. Garcke, and R. Numberg, Numer. Methods Partial. Differ. Equ. **27**, 1 (2011).
[44] J. W. Barrett, H. Garcke, and R. Numberg, Numer. Math. **120**, 489 (2012).